5
Characterization and Modification of Electrode Surfaces by *In Situ* STM

Dieter M. Kolb and Felice C. Simeone

5.1
Introduction

Structure–reactivity relations are among the key issues both in electrocatalysis and in heterogeneous catalysis [1, 2]. Hence, determining the structure of an electrode surface, which shows a given catalytic activity, is an important goal in electrochemistry, and likewise, tailoring the structure of electrode surfaces for maximum catalytic output has been a long-lasting desire. The routine use of single-crystal electrodes with structurally well-characterized surfaces laid the basis of structure–reactivity studies in electrochemistry [3]. However, while well-prepared flat single-crystal surfaces, preferably with the three low-index crystallographic orientations, tremendously increased our understanding of structure effects in adsorption reactions, it was quite clear that truly catalytic reactions will occur preferentially on surface defects. The latter, however, will escape detection by diffraction techniques, the commonly employed method to determine the structure of single-crystal surfaces. In this respect, scanning tunneling microscopy (STM) like its related scanning probe techniques plays an important role for catalysis because of their inherent ability to image surfaces in real space rather than in *k*-space. Under very special conditions, surfaces may be imaged while the reaction of interest is ongoing. This is limited to reactions where at least one partner gives sufficient contrast to be detected by STM [4]. A typical example of this is metal deposition.

In the following section, we focus on imaging single-crystal electrode surfaces that are of relevance to electrocatalysis. We will first deal with flat, defect-free terraces as well as with more real surfaces with monoatomic high steps as the most common active sites. We will then explore various strategies for nanostructuring surfaces, for example, by repetitive oxidation–reduction cycles (ORCs).

Soon after the invention of the STM as a tool for imaging surfaces in real space, it was discovered that the microscope could also be used (or misused) for surface manipulations, that is, for nanostructuring of surfaces [5]. The extremely close vicinity of the STM tip and the sample surface required by the tunnel process

Scanning Tunneling Microscopy in Surface Science, Nanoscience and Catalysis
Edited by Michael Bowker and Philip R. Davies

ISBN: 978-3-527-31982-4

inherently leads to an overlap of both electric double layers and hence to a tip influence on the surface processes under study. This seemingly undesirable drawback of tunnel microscopy is frequently employed for nanostructuring with hitherto unprecedented precision. While imaging bare and adsorbate-covered electrode surfaces, even with atomic resolution, has become a routine procedure, measuring electrochemical activities, that is, reaction currents, with a similarly high lateral resolution, still needs to be achieved. In this respect, scanning electrochemical microscopy (SECM) shows promise in accomplishing this goal in the near future. Since SECM is not the subject of this chapter, the interested reader is referred to a recent review [6].

5.2
In Situ STM: Principle, Technical Realization and Limitations

5.2.1
Principle Considerations for *In Situ* Operation

The principle of STM is well described in this book as well as in many other monographs [7–9]. In brief, a fine metal tip is brought into close proximity of the surface under study, typically 0.5–2.0 nm, so that the electrons can tunnel from one side to the other when a voltage U_T is applied between the tip and the sample (Figure 5.1). Then, the tip is scanned across the surface with either the tunnel current kept constant via a feedback circuit ("constant current mode") or the height of the tip kept constant ("constant height mode") [8]. In the first case, which is the commonly used one, the surface topography is reflected in the voltage applied to the *z*-piezo

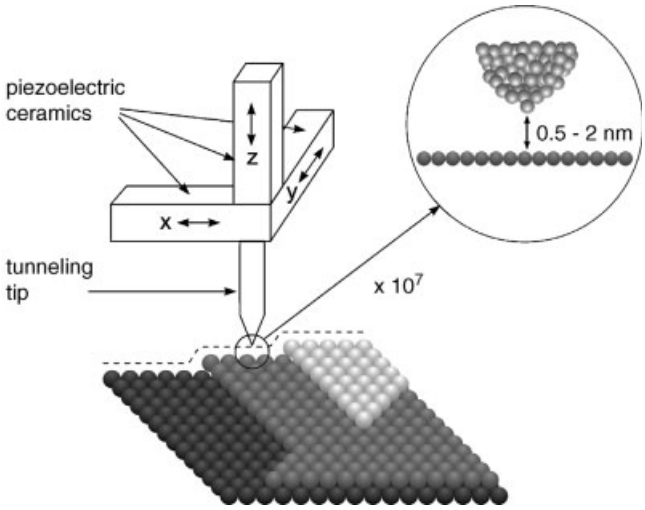

Figure 5.1 Schematic diagram showing the principle of STM.

(z being the direction normal to the surface) in order to keep the tunnel distance s constant. In the second case, the surface topography can be obtained from the variation of the tunnel current. The exponential dependence of the tunnel current on the tunnel gap s is the reason for the extreme height sensitivity of the STM, which allows detecting height variations in the 0.01 nm range and below. The lateral resolution, of course, is considerably lower, the exact value depending on the tip shape. The image of single (nonperiodic) events, such as monoatomic high steps, is usually smeared out by tip shape convolution over 1–2 nm. Nevertheless, periodic structures with 0.3 nm distances like that from individual atoms of a single-crystal surface can be clearly imaged [10].

One has to keep in mind that STM images show contours of constant tunnel probability rather than height contours directly. Nevertheless, for simple cases such as a metal surface, both quantities are closely related to each other. The dependence of the tunnel current I_T on the tunnel voltage U_T and on other parameters is given for the ideal case in Eq. (5.1):

$$I_T = R_0^{-1} U_T \exp(-A\sqrt{\phi_T}s), \tag{5.1}$$

where ϕ_T is the tunnel barrier, $R_0 = 12.90\,\mathrm{k\Omega}$ is the resistance of a point contact, and $A = 10.25\,\mathrm{eV}^{-1/2}\,\mathrm{nm}^{-1}$ [11].

The joint density of states (JDOS) for the electrons in the tip and the sample enter the equation for I_T, and hence in principle, STM images contain some chemical information about the imaged species. For all practical purposes, however, it is fair to state that STM does *not* yield chemical information because such information is very indirect and often heavily masked by topographic effects. This statement holds primarily for electrochemical systems, and also for a great deal of the UHV studies, although there are a few very beautiful examples presented in the literature that demonstrate a clear chemical contrast for different atomic species of bimetallic surfaces [12–14]. Since for electrochemical systems, potential limitations (e.g., due to hydrogen evolution or tip oxidation) severely restrict the application of scanning tunneling spectroscopy (STS), chemical information can hardly be derived using an STM. Additional methods, such as cyclic voltammetry, *in situ* SXRD or even *ex situ* XPS, and Auger electron spectroscopy, are often crucial for a safe assignment of features in the STM image.

Although the tunnel barrier ϕ_T varies with the tip–sample distance s, it resembles the local work function of the surface for the large s, but the numbers for an electrochemical environment are substantially different from those for UHV conditions. For metal electrodes in aqueous solution and $s > 1$ nm, tunnel barriers range between 1.0 and 2.0 eV, $\phi_T = 1.5$ eV being a typical value [15]. However, while for metals in UHV or in air and $s < 0.5$ nm, the tunnel barrier increases almost linearly from zero at point contact to a constant maximum value [16], ϕ_T *in situ* shows a very characteristic, potential-dependent variation with s, from which structure information about the electrochemical interface normal to the metal surface can be extracted [17]. A result from the so-called distance tunneling spectroscopy, $I_T = f(s)$ at $U_T = \mathrm{const}$, is given in Figures 5.2 and 5.3. From a simple visual inspection of the various exponential decays of I_T with increasing tip–sample distance s for

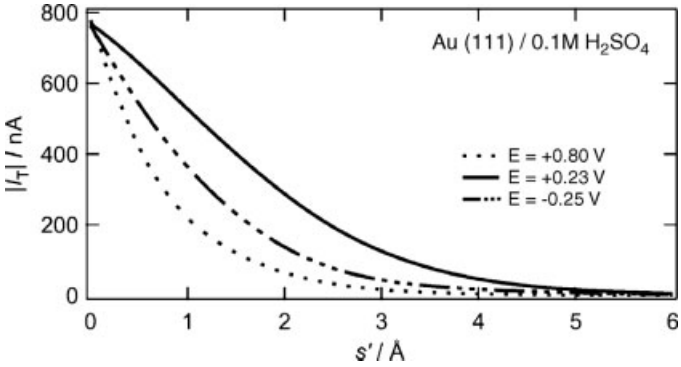

Figure 5.2 Tunnel current as a function of tip–sample distance for Au(1 1 1) in 0.1 M H_2SO_4 for three different electrode potentials (vs. SCE): Positive of (· · ·), negative of (– · · · –), and at the pzc (—). $s' = 0$ refers to the tip position at the closest approach that could be experimentally achieved. (Reproduced with permission from Ref. [19].)

different electrode potentials, it becomes evident that the tunnel barrier markedly depends on the electrode potential. A quantitative evaluation of ϕ_T via Eq. (5.2)

$$\phi_T(s) = \frac{\hbar^2}{8m}\left(\frac{\mathrm{d}\ln I_T}{\mathrm{d}s}\right)^2 \tag{5.2}$$

for three different electrode potentials is shown in Figure 5.3 [18, 19]. The three cases refer to potential values, positive and negative of the potential of zero charge (pzc) and at the pzc. An oscillatory behavior of ϕ_T is observed on either side of the pzc, that is, when the ions of the supporting electrolyte build up the solution side of the electric double layer. With the help of *ab initio* DFT calculations, the maxima and minima of the tunnel barrier could be related to positive and negative excess charge densities and hence to the positions of ions in the double layer [18, 19]. At the pzc, that is, in the absence of any excess charge, and hence in essence in the sole presence of water, the barrier height varies with distance from the surface like for metal/air interfaces. These results emphasize once more the importance of ions in determining the electrochemical interface properties.

For *in situ* investigations of electrode surfaces, that is, for the study of electrodes in an electrochemical environment and under potential control, the metal tip inevitably also becomes immersed into the electrolyte, commonly an aqueous solution. As a consequence, electrochemical processes will occur at the tip/solution interface as well, giving rise to an electric current at the tip that is superimposed on the tunnel current and hence will cause the feedback circuit and therefore the imaging process to malfunction. The STM tip *nolens volens* becomes a fourth electrode in our system that needs to be potential controlled like our sample by a bipotentiostat. A schematic diagram of such an electric circuit, employed to combine electrochemical studies with electron tunneling between tip and sample, is provided in Figure 5.4. To reduce the electrochemical current at the tip/solution

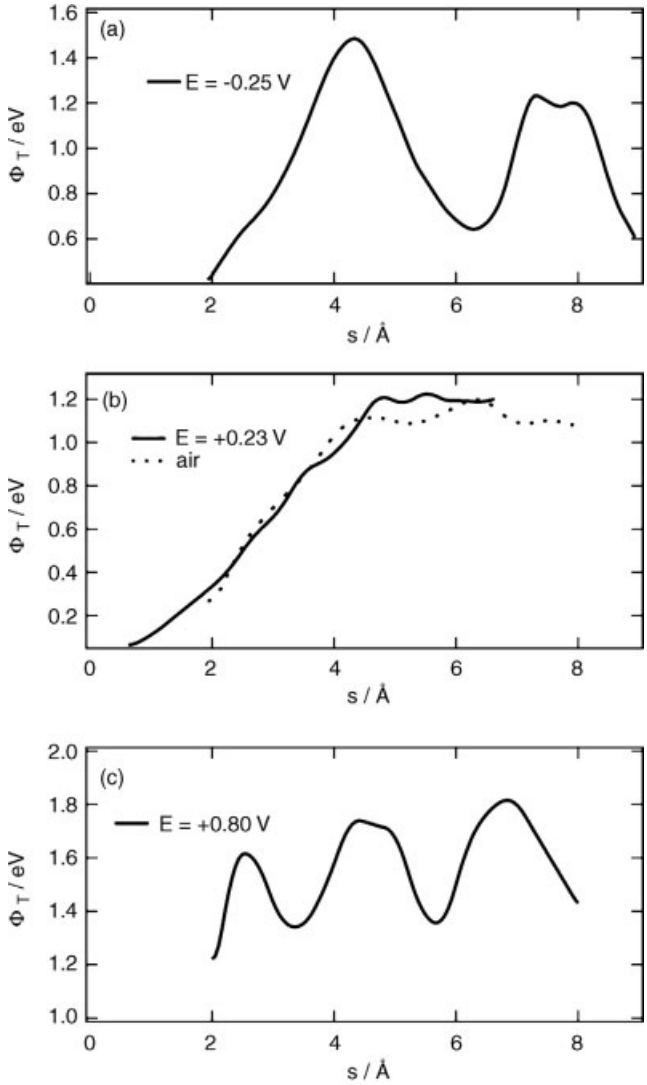

Figure 5.3 Tunnel barrier ϕ_T as a function of tip–sample distance for Au(1 1 1) in 0.1 M H_2SO_4 for three different potentials (vs. SCE). $s = 0$ refers to the surface plane of Au(1 1 1). ϕ_T (s) for Au(1 1 1) in air is also shown for comparison. For details see Refs [18, 19].

interface sufficiently enough to let the tunnel current control the feedback circuit of the microscope, two different actions have to be taken [20]: (a) the tip potential may be chosen such that it is close to its rest potential and (b) the area of the tip exposed to the electrolyte has to be reduced as much as possible by an appropriate isolation (see Section 5.2.2.1).

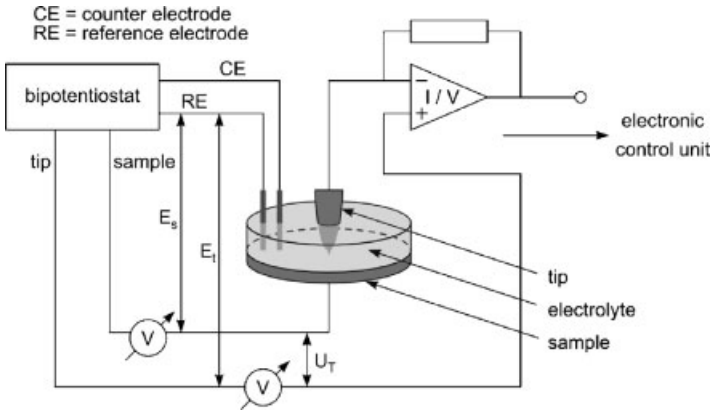

Figure 5.4 Electric circuit for *in situ* STM, which allows sample and tip potentials to be controlled independent from each other.

5.2.2 Technical Realization

While the first STM studies of electrode surfaces were performed with self-built instruments, scanning tunneling microscopes for electrochemical use are nowadays commercially available at a price that hardly justifies the effort of homemade equipment. Nevertheless, new instrumental designs are now and then discussed in the literature, which are still worthwhile to be considered for special applications. There is, however, additional equipment required for the operation of an electrochemical STM, for which homemade designs may be advantageous over commercially available ones and hence is briefly mentioned here in terms of tip preparation and isolation, the electrochemical cell, and vibration damping.

5.2.2.1 Tip Preparation and Isolation

Very fine tips are required for high lateral resolution. The most commonly used tip materials are tungsten and a platinum–iridium alloy (80 : 20). Tips are manufactured by electrochemical etching of a 0.25 mm thick wire in a lamella of solution (Figure 5.5) [21]. For W tips, the solution consists of 2 M NaOH (etching at 2.4 V DC), for Pt:Ir tips 3.4 M NaCN is used (and 4.2 V AC). For tungsten, both parts can be used as tips, while with Pt:Ir only the lower part is suitable for high-quality imaging. While from an electrochemical point of view, Pt:Ir tips are easier to handle, their potential range of stability being clearly larger than that for tungsten, W tips are sharper and yield better images. Atomically resolved images are preferably obtained from tungsten tips. We mention in passing that according to literature, Pt:Ir tips were frequently produced by simply cutting the wire with a pair of pliers, with reasonably good success as far as imaging is concerned. According to our experience, tips produced in this way are not very suitable for electrochemical studies, but we have used such tips for imaging surfaces in air. It seems important to cut the wire while it is being pulled.

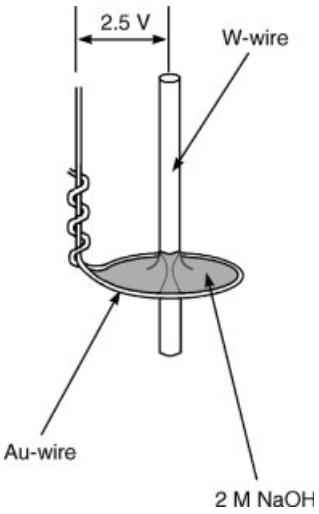

Figure 5.5 Setup for the tip production by electrochemical etching of a tungsten wire. (Reproduced with permission from Ref. [21].)

For *in situ* STM measurements, the tip is inevitably immersed into the electrolyte and acts as a fourth electrode with reactions occurring at the tip–electrolyte interface. To reduce the electrochemical current at the tip to a size well below the tunnel current at the tip, the area in contact with the solution must be reduced by coating the largest portion of the STM tip with an insulating layer. In the literature, various ways of insulating the tip have been described. In the past, Apiezon®, a chemically very inert thermoplast, has been used with success [22, 23], but at present, electrophoretic paints are widely employed for tip insulation [24]. In both cases, the uncoated part of the tip is about 1 μm or less, leaving an area in contact with solution of the order of 10^{-8}–10^{-7} cm^2. The remaining electrochemical currents are generally smaller than 50 pA (which is below the detection limit of commercial STM potentiostats), and they no longer interfere with the imaging process. Besides the reduction of the electrochemically active area of the tip, the proper choice of the tip potential can also help in minimizing Faradaic currents through the tip/electrolyte interface. This requires the use of a bipotentiostat, which allows one to choose the tip potential independent of the sample potential with respect to a common reference electrode. Such a bipotentiostat is supplied by most STM manufacturers. It enables one to select a tip potential close to the rest potential of the tip, where by definition no Faradaic currents should flow. While this precaution was indeed necessary a few years ago, the tip insulation has meanwhile progressed to a point, where restrictions of the tip potential to values close to the rest potential are no longer necessary. This has been an important advancement because with a freely chosen tip potential, scanning tunneling spectroscopy becomes feasible, albeit in a very limited potential region dictated by the decomposition of water or the stability of the tip material against anodic oxidation.

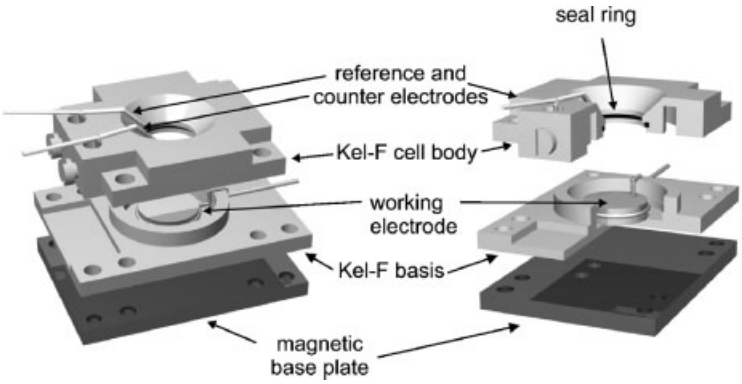

Figure 5.6 Electrochemical cell design as used in the authors' laboratory for STM.

5.2.2.2 **Electrochemical Cell**

The design of the electrochemical cell is largely determined by (a) the shape of the single-crystal electrodes to be studied and (b) the stringent requirements for a thorough cleaning before its use. The design of our electrochemical STM cells is shown in Figure 5.6. All parts are made of Kel-F, which is easy to clean and which resists strongly oxidizing agents, such as caroic acid (conc. H_2SO_4 + 30% H_2O_2), and the cell is designed for single-crystal disks of about 10 mm diameter and 2 mm thickness. Since only the polished face of the single-crystal disk is in contact with the electrolyte, electrochemical experiments can in principle be performed in the STM cell, for example, for surface characterization by cyclic voltammetry. However, one has to keep in mind that the cell has been optimized for STM use rather than for electrochemical experiments and accordingly two major deficiencies prevent one from obtaining high-quality cyclic voltammograms, routinely recorded in normal electrochemical cells: (a) the STM cell is usually open to air, hence oxygen reduction distorts the current–potential curves and (b) it normally takes minutes to assemble the STM cell, which creates contamination problems. Consequently in most cases, STM images and the corresponding electrochemical characterization are obtained in different cells and different experiments.

The electrolyte volume of the STM cells is usually very small (of the order of a 100 µl in the above-described case) and evaporation of the solution can create problems in long-term experiments. Miniature reference electrodes, mostly saturated calomel electrodes (SCE), have been described in the literature [25], although they are hardly used anymore in our laboratory for practical reasons: Cleaning the glassware in caroic acid becomes cumbersome. For most studies, a simple Pt wire, immersed directly into solution, is a convenient, low-noise quasireference electrode. The Pt wire is readily cleaned by holding it into a Bunsen flame, and it provides a fairly constant reference potential of $E_{Pt} = +0.55 \pm 0.05$ V versus SCE for 0.1 M sulfuric or perchloric acid solutions ($+0.67 \pm 0.05$ V for 0.1 M nitric acid), which has to be checked from time to time and for different solutions.

5.2.2.3 Vibration Damping

It is obvious from the principle of STM that the microscope has to be shielded from mechanical and acoustic vibrations of the outside world as much as possible to achieve good imaging quality, particularly if atomic resolution is required. After all, there are two macroscopic parts – tip and sample – that are only fractions of a nanometer apart, and this distance needs to be controlled within hundredths of a nanometer. Experience has shown that vibrations of the building with frequencies below 10 Hz are especially critical, that is, difficult to eliminate. A simple, yet very effective construction for vibration damping is described in Ref. [26]. It consists in essence of two platforms, a very heavy stone plate (about 200 kg) and a light one (e.g., a wooden board, onto which the STM rests), suspended on metal frames with springs that have vastly different force constants [27]. Needless to say that the preferred location for setting up an STM is the basement rather than the top floor of a building. The microscope is placed in a little Faraday cage, lined with foam rubber for damping acoustic waves.

5.2.3 Limitations

Possible limitations in the use of STM arise from the close proximity of the tip to that part of the sample that is imaged. Under normal imaging conditions, for example, $I_T = 2$ nA and $U_T = 50$ mV, the tip–substrate distance s can be estimated from Eq. (5.1) to be around 0.6 nm (with $\phi_T = 1.5$ eV [15]). Considering the fact that the electric double layer of a metal electrode in concentrated solution is about 0.3 nm thick [28, 29], the double layers of tip and substrate begin to merge and the ideal picture of a noninteracting tip is no longer valid under these conditions. For example, contact with the reference electrode for the imaged area right underneath the tip may be lost because the bulk electrolyte that carries the reference potential has been squeezed out. It has been shown that a Cu surface can be locally corroded right underneath the tip if a positive potential is applied to the tip rather than to the sample [30]. Another disturbance brought about the STM tip is the so-called tip shielding [31]. Considering a typical tip radius of a few tens of nanometers, tip and sample constitute an extreme example of a thin-layer cell with restricted diffusion of reactants to the imaged area (e.g., metal ions in metal deposition studies) and with iR-drops distorting the externally applied electrode potential. Hence, great care must be exercised when treating kinetic data acquired by an STM as absolute; the mere presence of the tip under tunneling conditions can strongly affect the kinetics of a reaction.

Finally, some requirements with respect to the substrates under study should be mentioned. One may notice that practically all STM studies are performed with single-crystal electrodes and not with (industrially more relevant) polycrystalline samples. For one, this certainly has something to do with the high lateral resolution that the STM offers and the researcher wants to make use of. Rough surfaces would be too demanding for a feedback circuit, capable of reacting to atomic heights. Since mechanistic interpretations of electrochemical reactions require well-defined surface structures and atomically resolved images of bare and adsorbate-covered

electrodes, one has to retreat to single-crystal electrodes. However, the STM-derived structure information stems from a tiny area of the electrode, typically 100 nm × 100 nm, and needs to be compared with electrochemical data that inevitably represent the whole macroscopic electrode surface. Such a relation will be meaningful only if the structure information holds for the whole electrode surface. This is the case only for high-quality single-crystal surfaces.

5.3 Imaging Single-Crystal Surfaces of Catalytically Relevant Systems

5.3.1 Preparation and Imaging of Metal Single-Crystal Surfaces

Mechanistic interpretations of electrochemical processes, which involve adsorption of reaction intermediates or products, require in general the use of single-crystal electrodes with structurally well-defined surfaces. Classical examples are the oxidation of small organic molecules such as formic acid [32] or the underpotential deposition of metals [33, 34]. In the 1970s, right at the beginning of "electrochemical surface science," single-crystal surfaces were prepared in a UHV chamber by sputtering and annealing, and their structure and cleanliness checked by electron diffraction and AES [35–37]. This was a rather cumbersome approach for electrochemists and limited the use of well-characterized electrodes to those groups that had access to surface science equipment. A significant advancement of single-crystal electrochemistry came with the so-called flame-annealing technique, which required in essence only a Bunsen burner to prepare clean and well-ordered surfaces, as first demonstrated by Clavilier *et al.* for platinum [38] and later by Hamelin for gold [39]. Although the initial advice of the French school, to quench rapidly the still hot crystal in water to reduce the danger of surface contamination as much as possible, had to be abandoned because the heat shock turned out to be detrimental to the bulk crystallinity, the resulting surface quality in retrospect has to be considered high. For platinum, which is particularly sensitive to contamination from air, cooling in an iodine [40] or CO [41] atmosphere was advocated, the adsorbed layer protecting the surface extremely well during transfer to the electrochemical cell and being finally removed from the surface by oxidative desorption. Ultimately, inductive heating in a reducing atmosphere turned out to be the best choice as this technique allows the preparation of clean and well-ordered surfaces of reactive metals such as Cu, Ag, Pd, Rh, and Ru for which the by now classical flame-annealing in ambient atmosphere has failed. This is particularly true for large single-crystal electrodes, commonly employed for spectroscopic studies, which due to their higher heat capacity require longer cooling times. Details of the technique can be found in Ref. [42]; a schematic diagram is given in Figure 5.7.

The devastating influence of trace amounts of oxygen during cooling on the quality of a Pt single-crystal surface is demonstrated in Figure 5.8, where the STM images of Pt(1 1 1) in 0.1 M H_2SO_4 after cooling down the crystal in air and in hydrogen

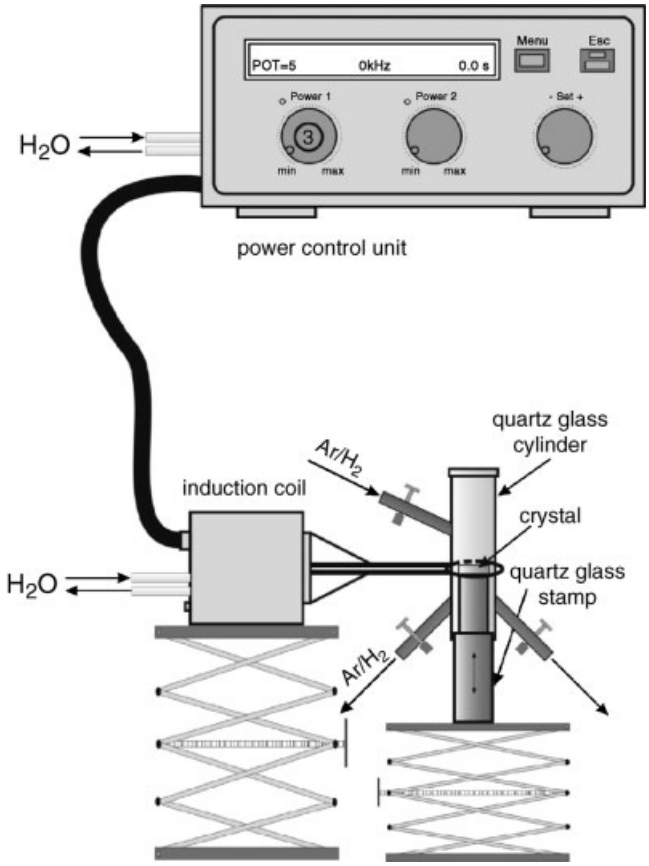

Figure 5.7 Setup for the inductive heating of single-crystal electrodes in controlled atmosphere.

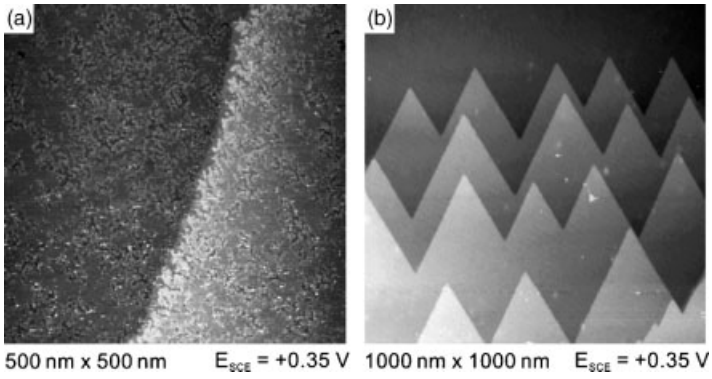

Figure 5.8 STM images of Pt(1 1 1) in 0.1 M H_2SO_4 at $+0.35$ V versus SCE, after cooling the sample in air (a) and in H_2 (b). (Reproduced with permission from L.A. Kibler, personal communication.)

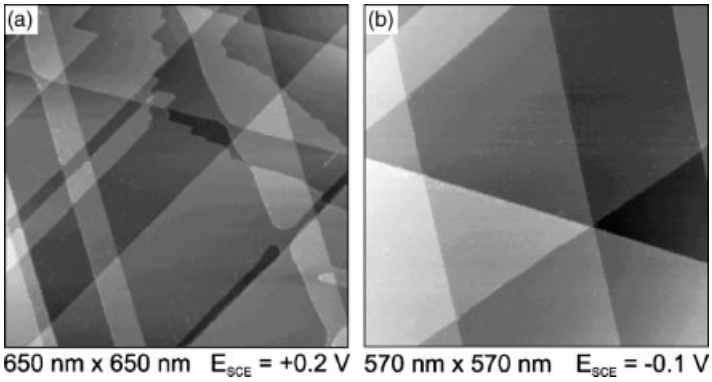

Figure 5.9 STM images of (a) Pd(1 1 1) in 0.01 M H_2SO_4 and (b) Rh(1 1 1) in 0.1 M H_2SO_4. Both crystals were annealed in a H_2-flame and cooled in H_2. (Reproduced with permission from Ref. [43].)

are compared (L.A. Kibler, personal communication). While cooling in air leads to a rough surface, cooling in a reducing atmosphere such as H_2 or H_2/Ar mixtures yields large, atomically flat terraces. Other examples of well-prepared single-crystal surfaces are given in Figure 5.9, which shows Pd(1 1 1) and Rh(1 1 1) in 0.1 M H_2SO_4 [43].

Quite often atomically resolved *in situ* images of single-crystal surfaces are desirable because they would allow a precise length calibration of the piezos. However, zooming with the microscope into the terraces, one frequently images anion adlayers rather than the metal surface proper. Although interesting in their own right, these adlayers prevent direct viewing of the substrate. Sulfate, chloride, and metal chloro complexes are well known to form ordered adlayers [44], at least at high coverages, which are easy to image by STM with molecular resolution. Examples thereof are given in Figure 5.10 [45–48].

5.3.2 Bimetallic Surfaces

Bimetallic surfaces, either alloys or a metal A onto which a metal B was deposited in submonolayer amounts, play an important role in electrocatalysis. For their structural characterization, a chemical contrast in the STM images would be highly desirable. So far, however, the number of such examples is vanishingly small, and in almost all cases, one has to rely on morphological (height) contrast. A rare example of a system showing chemical contrast is Pd and Au as has been demonstrated for Pd deposits on Au(1 1 1) [49] as well as for Pd–Au alloy surfaces [50]. When Pd is deposited from aqueous solution onto Au(1 1 1), nucleation starts exclusively at the monoatomic high steps of the substrate, followed by a two-dimensional growth of the Pd onto the lower terrace. Figure 5.11 shows the growth of a Pd layer that had nucleated at the rim of a monoatomic high gold island. Although the monolayers of both metals should have about the same height (the Pd layer being slightly lower, if at all), the gold island appears darker in the STM image than the surrounding Pd.

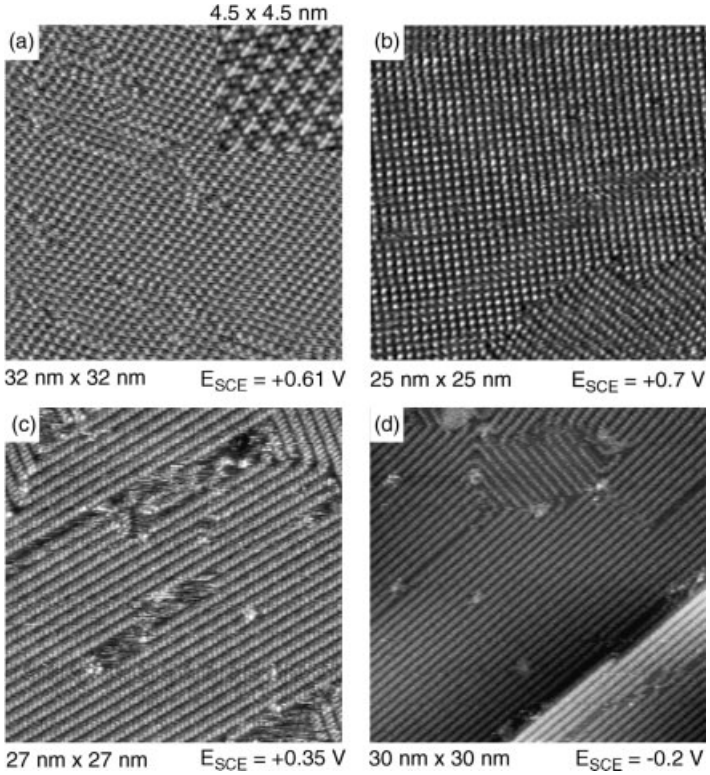

Figure 5.10 STM images of ordered anionic adlayers. (a) $PdCl_4^{2-}$ on Au(1 0 0) in 0.1 M H_2SO_4 + 0.1 mM H_2PdCl_4 + 0.6 mM HCl [45]; (b) $PtCl_4^{2-}$ on Au(1 0 0) in 0.1 M H_2SO_4 + 0.1 mM K_2PtCl_4 [46]; (c) sulfate on Au(1 0 0) in 0.1 M H_2SO_4 [47]; (d) sulfate on Ag(1 0 0) in 0.1 M H_2SO_4 [48].

This chemical contrast may be due to electronic effects or caused by differences in anion adsorption on both metals. Evidence for electronic effects as possible origin of the chemical contrast between Pd and Au has been presented in STM images of Pd/Au alloy surfaces with atomic resolution, which allowed an identification of Pd or Au atoms on the basis of their brightness [50]. A similar picture is presented in Figure 5.12 showing the surface of a $Pt_{50}Ru_{50}$ alloy [43]. There are atoms that appear clearly brighter (about 0.04 nm higher), which in accordance with UHV–STM investigations [51, 52] could be assigned to Ru because of its higher electron density at the Fermi level. Their number, however, is much smaller than that of the Pt atoms, indicating a marked difference between bulk and surface composition of the alloy. Indeed, the corresponding cyclic voltammograms recorded in 0.1 M H_2SO_4 reveals a surface that is almost Pt(1 1 1)-like. From the image in Figure 5.12 it is concluded that the Ru atoms are more or less uniformly distributed over the surface and only small assemblies are formed. We mention in passing that cooling the $Pt_{50}Ru_{50}$ single-crystal alloy after inductive heating in a reducing atmosphere yields the Pt-rich

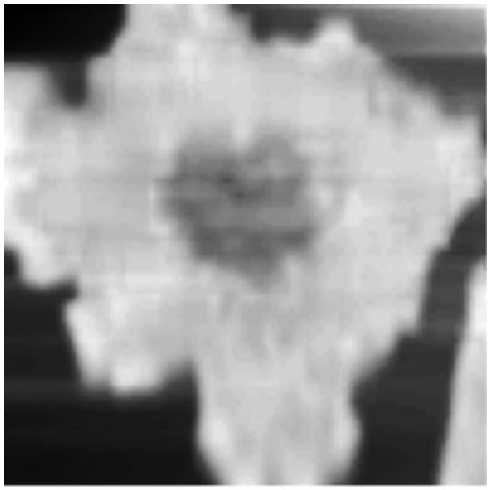

Figure 5.11 STM image of a growing Pd monolayer, which had nucleated on Au(1 1 1) at the rim of a gold island. Although practically equal in height, the Pd layer appears brighter than the gold island in the center. (Reproduced with permission from Ref. [49].)

surface, whereas cooling in an inert (Ar) atmosphere with traces of oxygen leads to a Ru-rich surface [53, 54].

From the image in Figure 5.12 one may guess how difficult the measurements and how limited the systems are that show a true chemical contrast. In most cases, one has to retreat to the morphological information in order to assign features to metal A or metal B. This is routinely done in metal deposition studies that start with an image of the bare surface, followed by the ones with the metal deposit at various stages, that is, various amounts. Numerous examples are given in the literature [26, 55, 56], one being reproduced in Figure 5.13. It shows Pt electrodeposited onto Au(1 1 1), the little hillocks on a flat substrate being easily identified as the Pt clusters [46]. With this image another well-established observation is confirmed: Nucleation starts preferentially at surface defects, the growing nuclei decorating the substrate's defect structure.

5.4
Strategies for Nanostructuring Surfaces

5.4.1
Oxidation–Reduction Cycles for Roughening and Faceting Surfaces

The dominance of surface defects over terrace sites in catalysis and electrocatalysis had been recognized already in the early stages of surface science. For example,

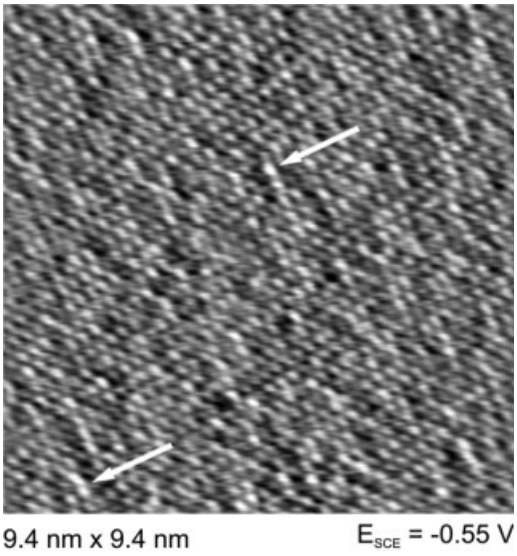

Figure 5.12 Atomically resolved STM image of a $Pt_{50}Ru_{50}$(1 1 1) alloy electrode in 0.01 M NaF after annealing and cooling in H_2/Ar. The arrows mark bright spots that are assigned to Ru atoms. (Reproduced with permission from Ref. [43].)

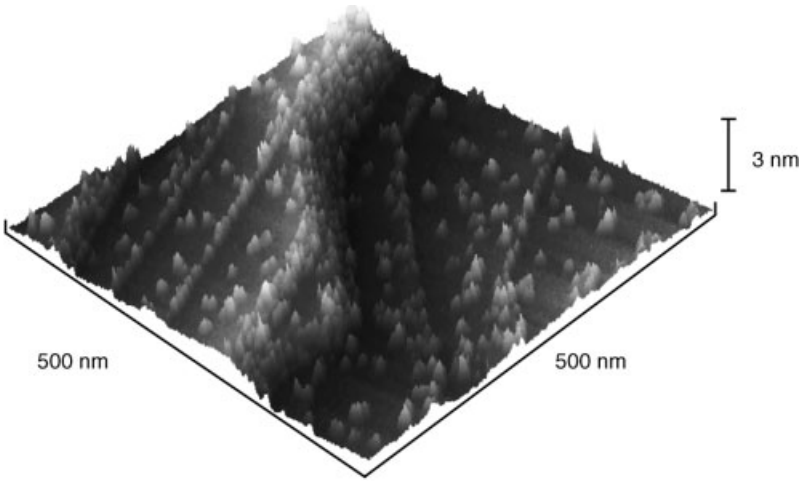

Figure 5.13 STM image of Pt clusters electrodeposited onto Au(1 1 1) in 0.1 M H_2SO_4 + 0.1 mM K_2PtCl_4. $E = +0.1$ V versus SCE. (Reproduced with permission from Ref. [46].)

stepped single-crystal surfaces were used to make the role of monoatomic high steps in the substrate visible [57]. Likewise, surfaces with a regular roughness, that is, surfaces covered with islands or clusters of a narrow size distribution, may serve as model systems, for which size-reactivity relations can be derived.

The application of oxidation–reduction cycles, repetitively applied to an electrode to create rough or facetted surfaces, has a long tradition in electrochemistry [58–62]. Particularly worth noting are the works of Arvia and his group [59, 60], in which faceting of polycrystalline Pt by ultrafast potential cycling has been described. It was shown that cycling in the kHz-region for an extended period of time (typically for about 1 h) caused either (1 1 1)- or (1 0 0)-type of facets to grow, depending on the negative and positive potential limits.

In a systematic study on the influence of conventional ORCs, that is, with scan rates on the order of 10–100 $mV\,s^{-1}$, on the surface structure of Au(1 1 1), it was demonstrated that slow potential cycling from the oxide formation region back to the reduced state caused monoatomic deep holes in the surface, whereas fast cycling or potential stepping led to clusters on the surface in addition to the holes [63]. The place exchange between metal and oxygen during oxide formation leads to metal adatoms on the surface upon oxide reduction. In the first case (slow potential cycling), the adatoms apparently are given enough time to be incorporated at nearby monoatomic high steps of the substrate (the Ehrlich–Schwoebel barrier would prevent them to fall into the advacancies), whereas the advacancies condense to vacancy islands (holes that are visible in STM images). Fast oxide reduction, for example, due to potential stepping leads to cluster formation on flat terraces because of the quickly established large supersaturation potential.

Repetitive potential cycling or stepping enhances the above-described effect and surface roughnesses emerge that should be of interest in the study of model catalysts. It has been demonstrated for gold that specifically adsorbing ions such as Cl^- drastically enhance surface diffusion, which is the basis of the so-called electrochemical annealing [64, 65]. Hence, by selecting the appropriate parameters for the ORC and choosing the right electrolyte composition, a tailoring of surface roughness seems feasible. Figure 5.14 shows the STM image of an originally flat Au(1 1 1) terrace, which was subjected to 100 potential cycles at 100 $mV\,s^{-1}$ between 0.7 and 1.3 V versus SCE in 0.1 M H_2SO_4. The clusters have an average height of six–eight layers (Köntje et al., in preparation).

5.4.2
Surface Modification by an STM: An Overview

Inspired by the amazing successes of surface scientists in nanostructuring surfaces with the tip of an STM, albeit at UHV conditions and often at low temperatures [66–68], electrochemists began to use an STM or AFM as a tool for nanostructuring electrode surfaces, mostly by spatially confined metal deposition. Figure 5.15 summarizes the various routes, which are currently employed in the community for electrochemical nanostructuring. In the following, we shall briefly address seven of them, and devote a separate chapter to the case sketched in

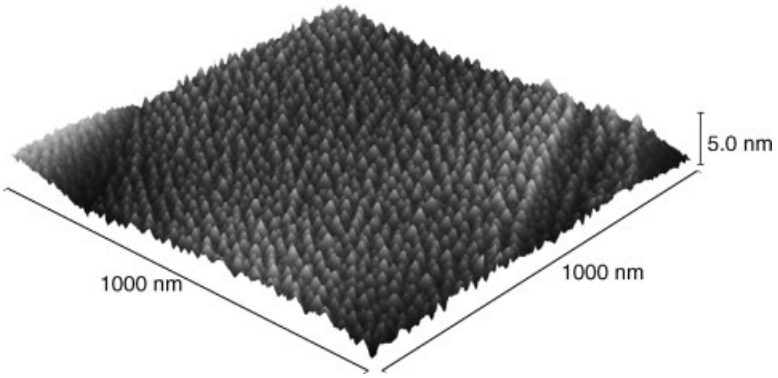

Figure 5.14 STM image of a Au(1 1 1) electrode, roughened by about 100 oxidation–reduction cycles at 100 mV s^{-1} in 0.1 M H_2SO_4. Cycling between 0.7 and 1.3 V versus SCE. Image taken at + 0.05 V versus SCE. (Reproduced with permission from Köntje *et al.*, in preparation.)

Figure 5.15h because this approach is intensively pursued in the authors' laboratory.

The first successful attempts of electrochemical nanostructuring, pioneered by Penner *et al.* [69], involved the generation of surface defects by the tip at predetermined positions, which were created either by a mechanical contact between tip and substrate (tip crash) or by some sort of sputtering process, initiated by high-voltage

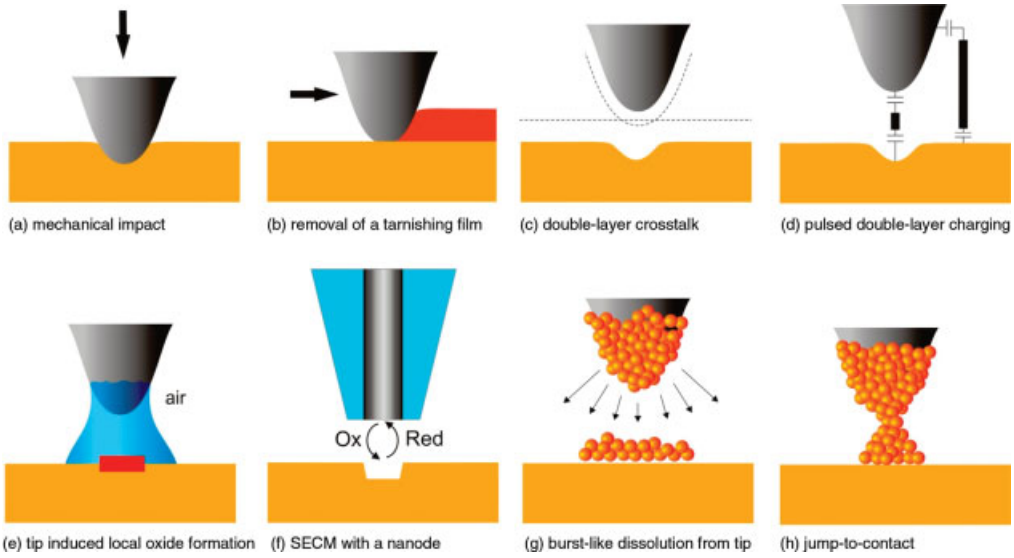

Figure 5.15 Various approaches to electrochemical nanostructuring with an STM, currently employed by the community.

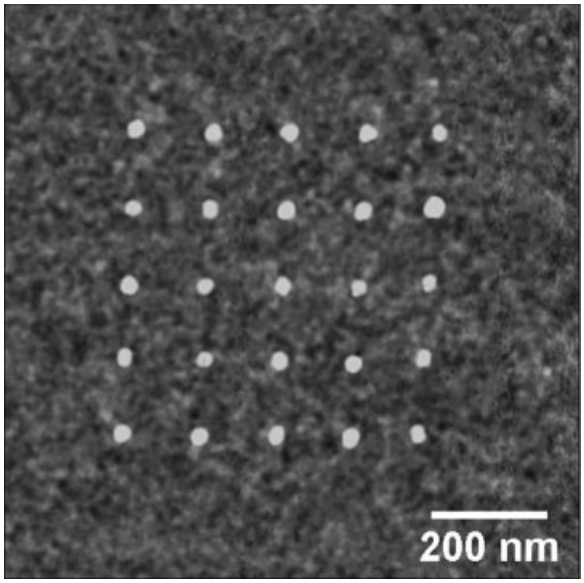

Figure 5.16 Tapping-mode AFM image of a 25 Cu nanodot array on H-terminated *p*-Si(1 0 0), formed by nanoindentation. (Reproduced with permission from Ref. [72].)

pulses applied to the tip [70]. These artificially created defects then acted as very effective nucleation centers for metal deposition, which allowed the decoration of electrode surfaces by metal clusters on a nanometer scale (Figure 5.15a). While in the beginning, this technique had been applied almost exclusively to metal substrates, studies were extended more recently to semiconductor surfaces. Impressive examples of patterned nanostructures made of metals such as Cu, Ag, or Au on silicon wafers were given by Homma *et al.* [71, 72]. In those cases, however, the defects that acted as nucleation centers were generally made by a nanoindentation process via an AFM tip (Figure 5.16).

A slightly different approach to spatially confined metal deposition, which is less harmful to the substrate, is sketched in Figure 5.15b. It is the local removal of an overlayer that causes a high overpotential for metal deposition. By choosing an electrode potential slightly negative of the Nernst potential, where no metal deposition will take place on top of the overlayer, deposition will immediately set in upon removal of the tarnishing film by the tip of an STM or AFM sliding across the surface, at the freed portion of the surface only. The applicability of this approach has been demonstrated in an AFM study for Cu deposition onto an oxide-covered Cu surface [73] and in an STM study for Cu deposition onto Au(1 1 1) covered by a monolayer of sodium dodecyl sulfate (SDS) [74]. Although the precision of the metal nanostructures generated in such a way was far from being satisfactory [74], this method again reveals the potential of decorating semiconductor surfaces with metal nanostructures, while so far the studies have been restricted to metal on

metal. This, however, will require suitable, preferably organic molecules, which will adsorb strongly enough on the semiconductor electrode to form a dense monolayer with sufficient inhibition for metal deposition, but which can be removed by the tip without damaging the substrate.

An obvious way of generating metal structures of nanometer dimensions via an STM tip is sketched in Figure 5.15g: It is the burst-like dissolution of metal from the tip, onto which it had been deposited from solution, and the redeposition onto the substrate within a narrow region directly underneath the tip [75]. In a systematic study by Schindler *et al.*, it was demonstrated how to achieve redeposition of the metal dissolved from the tip and at the same time prevent metal deposition from solution onto the substrate directly [76]. The key lies in the momentarily high metal ion concentration after the sudden metal dissolution at the tip that causes a more positive Nernst potential for the surface region underneath the tip. Figure 5.17 shows the STM image of two Pb clusters, about 3 nm in height, generated by the burst-like dissolution of Pb from the STM tip and by redeposition onto H-terminated n-Si(1 1 1) [77]. The potential of this technique lies in the ability to decorate semiconductor surfaces with metal clusters.

A conceptually different approach to nanostructuring electrode surfaces by tip-generated metal clusters is sketched in Figure 5.15h. This approach, which facilitates a so-called jump-to-contact between tip and substrate for generating metal clusters, has been developed by our group and will be described in more detail in Section 5.4.3.

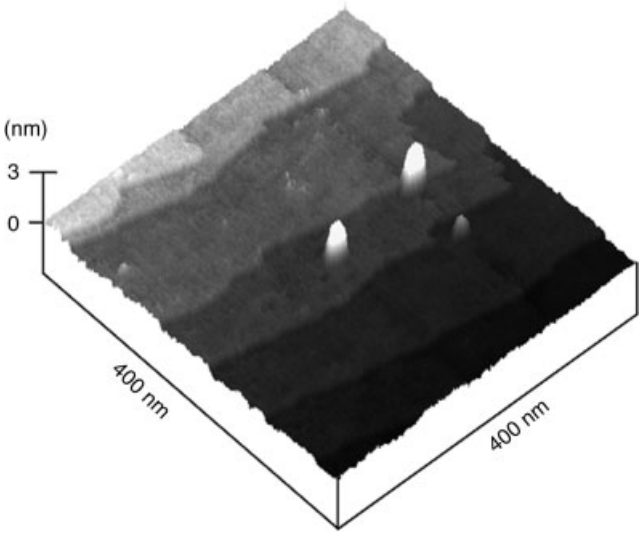

Figure 5.17 STM image of H-terminated n-Si(1 1 1) in 0.1 M $HClO_4$ + 1 mM $Pb(ClO_4)_2$, onto which two Pb clusters have been deposited by a burst-like dissolution of Pb from the STM tip. (Reproduced with permission from Ref. [77].)

The remaining methods sketched in Figure 5.15 either deal with spatially confined oxidation/dissolution of the substrate or describe means of studying electrochemical reactions on a nanometer scale.

We will first refer to what could be termed as double-layer crosstalk (Figure 5.15c). As mentioned already in Section 5.2.3, commonly employed tunnel parameters for imaging (e.g., $I_T = 2$ nA and $U_T = 50$ mV) lead to tip–substrate distances around 0.6 nm. This implies that the double layers of tip and substrate begin to merge, and the assumption of a noninteracting tip is no longer valid. For example, the close proximity of the tip may cause a change in potential for the imaged area directly underneath the tip because direct contact with the reference electrode is lost. It was demonstrated that spatially confined copper dissolution directly underneath the tip can be achieved by applying to the tip a potential positive of the Cu/Cu^{2+} reversible potential E_0, despite the fact that the sample potential was held clearly negative of E_0 [30]. Hence, copper was oxidatively dissolved by a tip–sample interaction underneath the tip and there only, although this process should not be possible at that sample potential. Later, this double-layer crosstalk was used to selectively dissolve Ag overlayers [78], demonstrating that this tip-induced metal dissolution is by no means restricted to Cu only as has been claimed in the literature [79]. It was also shown [30] that there is actually a smooth transition between imaging without much tip interference and tip-induced surface processing. Depending on the potentials of tip and sample, the following three regimes could be distinguished: (1) tip-enhanced copper deposition; (2) mere surface imaging; and (3) tip-induced copper dissolution.

In several publications, Schuster and coworkers have shown the use of STM tips (or other thin metal wires) as tools for electrochemical machining of electrode surfaces on a micrometer scale [80–82]. Spatially confined etching was achieved by applying nanosecond voltage pulses between tool and sample making use of the vastly different time constants for double-layer charging for different parts of the tool. As is sketched in Figure 5.15d, the variation of the time constant $\tau = RC$ for double-layer charging is solely due to the electrolyte resistance R, which increases tremendously when comparing that part of the tip (or tool) next to the sample surface with those higher up parts. The voltage pulse duration is now chosen in such a way that only for the forefront of the tool, that is, in a spatially very defined region, an electrode potential is established at the sample surface large enough for oxidative dissolution. In a series of impressive images, the viability of this route to electrochemical micro- and nanostructuring has been demonstrated (Figure 5.18).

A clever design for local oxide formation on silicon surfaces is depicted in Figure 5.15e. Operation of an STM in humid air leads to a neck of liquid due to capillary forces. Applying a voltage between tip and sample will trigger simple electrochemical processes in such a miniature electrochemical cell. Avouris *et al.* have used this method for pattering a Si surface with oxide [83].

The creation of nanostructured surfaces is one thing, the study of electrochemical reactions on such nanostructures is another one. Especially in electrocatalysis, where size effects on reactivity are often discussed, there have been attempts to use the tip of an STM as a detector electrode for reaction products from, say, catalytically active metal nanoclusters [84]. However, such ring-disk-type approaches are questionable,

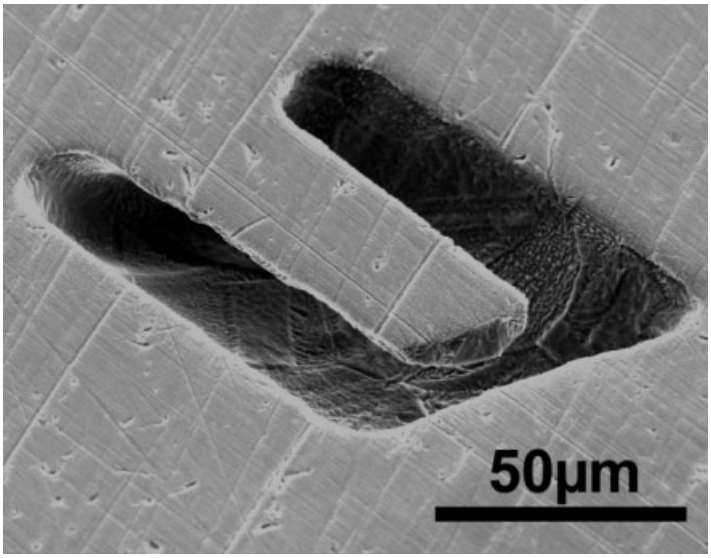

Figure 5.18 Scanning electron microscopy image of a microcantilever, electromachined into a stainless steel sheet by ultrashort voltage pulses (100 ns, 2 V, 1 MHz repetition rate) in 3 M HCl + 6 M HF. The tool electrode was a tiny loop of a 10 µm thick Pt wire. (Reproduced with permission from Ref. [80].)

when it comes to a quantitative analysis because of the ill-defined (if not to say unknown) geometry of the tip, which does not allow reliable mass transport calculations. On the other hand, scanning electrochemical microscopy has been demonstrated to ideally fulfill all these requirements, albeit on a micrometer scale [85, 86]. A major breakthrough in applying SECM for nanostructuring was achieved by Heinze and coworkers [87, 88], who developed Pt *nanodes* with active diameters down to 20 nm and glass insulation around them that ensure defined diffusion conditions, which are essential for a quantitative evaluation of reaction rates (Figure 5.15f). The potential of SECM for electrocatalytic studies on a nanoscale may even exceed that of the STM, provided the miniaturization of the electrodes will routinely reach the nanometer length scale. For a recent review, see Ref. [6].

5.4.3
Metal Nanocluster Deposition via Jump-to-Contact

Most of the work on nanostructuring electrode surfaces, which can be found in the literature, deals with the deposition of small metal clusters at predetermined positions. Over the years, we have developed a technique that is based on the "jump-to-contact" between tip and substrate [89] (Figure 5.15h) and that allows the formation of metal clusters in quick succession and without destroying the single crystallinity of the substrate. The principle behind this method is sketched in Figure 5.19 [90, 92]: By applying an electrode potential to the STM tip that is slightly

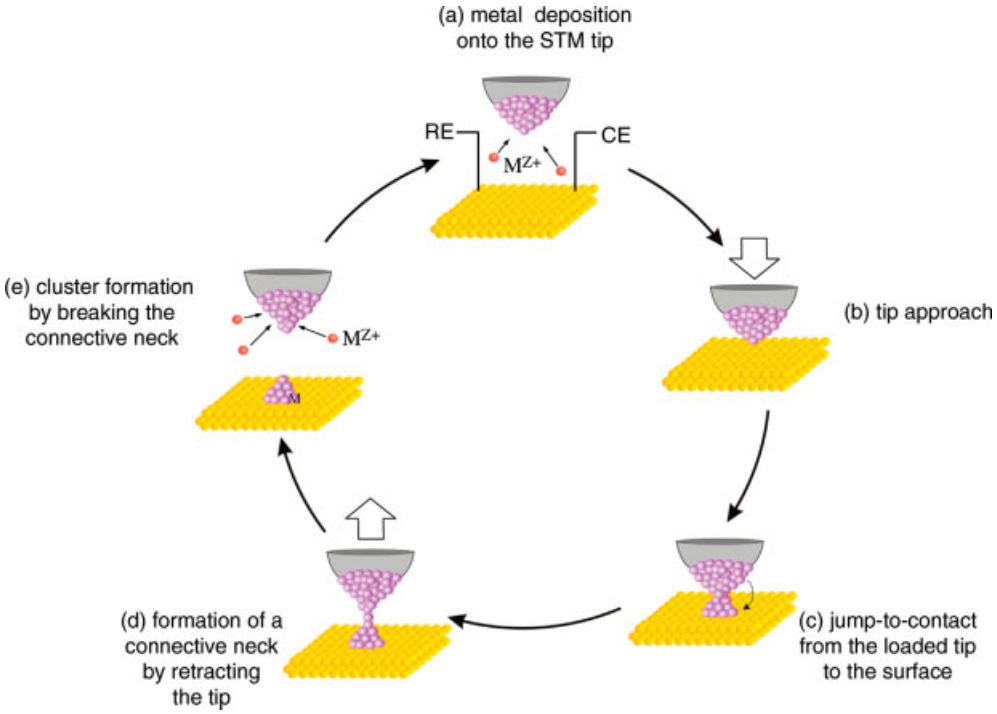

Figure 5.19 Schematic diagram for continuous cluster generation by the tip of an STM via jump-to-contact.

negative of the bulk deposition potential for the metal ions in solution, metal is deposited from the electrolyte onto the tip. Then, the metal-loaded tip is made to approach the surface close enough so that the jump-to-contact can occur. This leads to the formation of a connective neck, a metal bridge between tip and substrate, which will break upon the subsequent retreat of the tip, leaving a small metal cluster on the substrate surface. The tip is automatically "reloaded" because of the ongoing metal deposition and hence is ready for the next cluster formation.

The jump-to-contact requires an approach of the tip down to about 0.3 nm tunnel gap, which must be externally controlled. Actually, in our case all three spatial coordinates of the tip are externally controlled by a microprocessor, which makes the nanodecoration of an electrode surface with metal clusters a fully automated process, allowing even complex patterns to be fabricated rapidly and reproducibly. Two examples of tip-induced cluster formation are given in Figure 5.20, both referring to Cu on Au(1 1 1) in sulfuric acid solution [93]. Image (a) shows a circle of 12 Cu clusters on Au(1 1 1), all 0.8 nm in height. The pattern in image (b) not only proves the feasibility of complex structure formation but also demonstrates that monoatomic high steps in the substrate surface are no obstacles for nanostructuring, as the feedback control of the STM is not switched off. Although we have described various aspects of this method in a number of publications [91, 92], some technical details are briefly mentioned again for the sake of convenience:

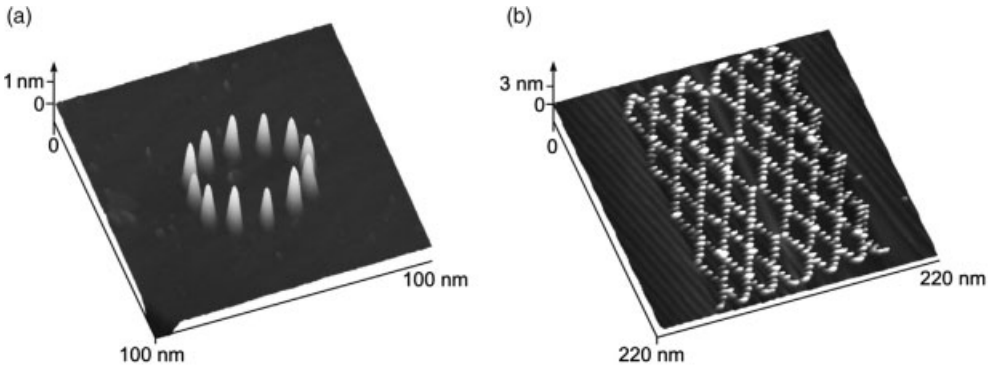

Figure 5.20 Two examples for the nanodecoration of a Au(1 1 1) electrode by tip-generated Cu clusters. Electrolyte: 0.05 M H_2SO_4 + 1 mM $CuSO_4$. (Reproduced with permission from Refs [90, 93].)

- If metal deposition is fast (as in the case of Cu in sulfuric acid solution), cluster generation can be performed at kHz rates. Obtaining an array of 10 000 Cu clusters on Au(1 1 1) takes a couple of minutes [15]. Typical parameters are 10–20 ms pulses at a rate of 50–80 Hz.
- Despite cluster formation via the STM tip, the imaging quality of the latter surprisingly remains high. Hence, writing and reading is possible with one and the same tip.
- The cluster size can be varied at will within a given range by changing the tip approach, the latter being controlled externally. Variation of cluster size with tip approach has been demonstrated for several metals on Au(1 1 1) [92, 94, 95].
- The high stability of the metal clusters allows one to hold the sample potential slightly positive of the Nernst potential, typically at + 10 mV versus Cu/Cu^{2+} in the case of copper. Thus, "normal" electrodeposition onto the sample directly from solution is prevented, whereas the tip-generated Cu clusters remain on the surface [96].
- Depending on the cohesive energies of cluster and substrate material, the jump-to-contact occurs from the tip to the substrate (e.g., for Cu and a gold electrode) or from the substrate to the tip (e.g., for Ni on the tip and a gold electrode) [93].
- So far, more than a dozen systems have been investigated and tested for nanostructuring [97]. While in the beginning most studies dealt with Cu clusters for testing and developing the method, our more recent work focused on Pd clusters for electrocatalytic investigations. A Au(1 1 1) surface with 12 arrays, each containing 2500 Pd clusters, is shown in Figure 5.21. Although such seemingly very large number of clusters are not sufficient for characterization by ordinary cyclic voltammetry, there may be a good chance to do so with an SECM, using a nanode that matches the cluster field in dimension.

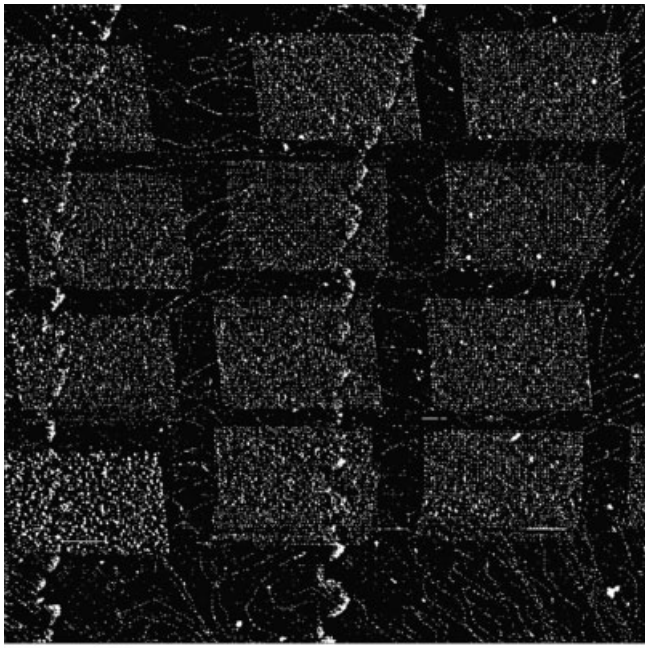

Figure 5.21 STM image of 12 cluster fields on Au(1 1 1), each field containing 2500 Pd clusters. Electrolyte: 0.1 M H_2SO_4 + 1 mM $PdSO_4$.

Two aspects deserve particular mention as they are of great practical relevance. The first deals with the unexpectedly high stability of the tip-generated clusters against anodic dissolution, which was briefly addressed above [96]. This is again demonstrated for Cu clusters on Au(1 1 1) in Figure 5.22, where the height of a tip-generated cluster is shown as a function of potential, as the latter is scanned from $+10$ mV versus Cu/Cu^{2+} to $+250$ mV. While bulk Cu would be quickly dissolved at an overpotential of 10 mV, and Cu upd is completely desorbed at $+250$ mV, the Cu cluster is still seen to exist, albeit at reduced height. Note that this information was obtained by scanning the tip in *x*-direction at constant *y*-position. Hence, a falsification of the potential values caused by possible tip-shielding effects can be ruled out. Although a reasonable explanation of the high cluster stability still has to be found, alloy formation as an obvious cause can safely be ruled out: Cluster dissolution brings back a perfectly flat, bare surface (see STM images in Figure 5.22 before and after anodic cluster dissolution [93]), whereas monoatomic deep holes are generally found on the surface for those cases where clusters did form an alloy with the substrate. The second aspect deals with room-temperature salt melts, the so-called ionic liquids (ILs), which open up many new and interesting perspectives for electrochemical studies [98]. The main advantage of ILs over aqueous solutions is their extremely wide stability range of almost 4 V, which has to be compared with the 1.23 V for water. Hence, electrodeposition of very unnoble, that is, reactive metals

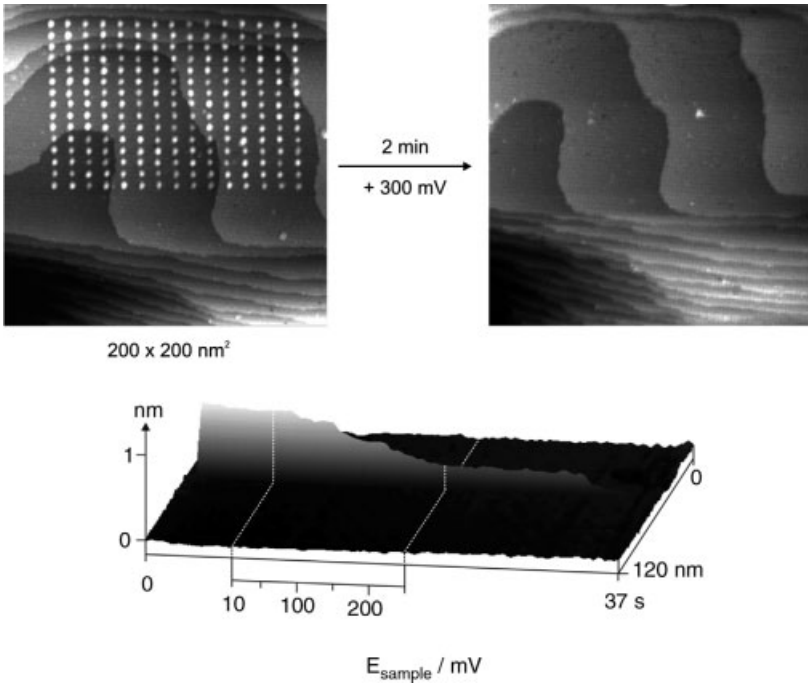

Figure 5.22 (a) STM image of an array of 225 tip-generated Cu clusters on Au(1 1 1) in 0.05 M H_2SO_4 + 0.1 mM $CuSO_4$. (b) Same area, but after dissolution of the Cu clusters at + 300 mV versus SCE. (c) Height of a single tip-generated Cu cluster as a function of potential and time, demonstrating the unusually high stability of the cluster against anodic dissolution. (Reproduced with permission from Ref. [93].)

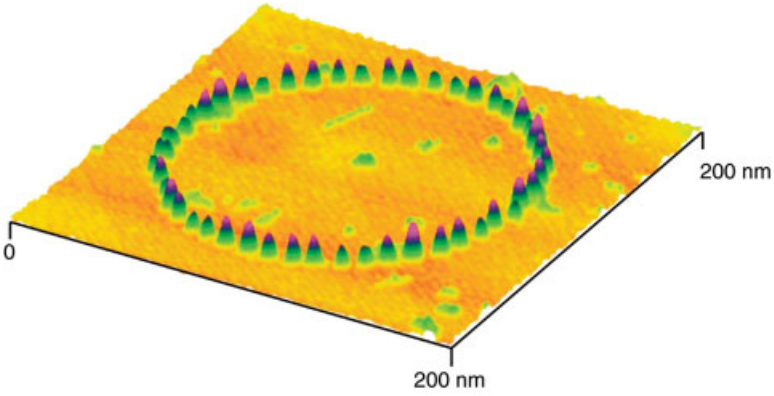

Figure 5.23 Ring of 48 tip-generated Fe clusters on Au(1 1 1) in 1-butyl-3-methyl-imidazolium BF_4 + approximately 50 mM $FeCl_3$. (Reproduced with permission from Ref. [95].)

such as Fe or Ta, becomes feasible. Even deposition of semiconductors such as Ge from ILs has been successfully demonstrated [99]. Tip-induced nanostructuring has also been performed in ILs [94, 95]. We end this chapter by showing a ring of Fe clusters generated on Au(1 1 1) in 1-butyl-3-methyl-imidazolium tetrafluoroborate, a typical and widely used IL, by jump-to-contact (Figure 5.23). Here again, the unusually high stability of the Fe clusters, which even exceeds that of upd Fe is noteworthy [95].

Acknowledgments

Parts of this work were supported by the Deutsche Forschungsgemeinschaft through SFB 569 and the Fonds der Chemischen Industrie. One of us (FS) gratefully acknowledges a stipend of SFB 569.

References

1 Trasatti, S. (ed.) (2003) Electrocatalysis: from theory to industrial applications. *Electrochim. Acta*, **48**, 3727–3974.
2 Ertl, G. (2008) *Angew. Chem. Int. Ed.*, **47**, 3524.
3 Markovic, N.M. and Ross, P.N. (2002) *Surf. Sci. Rep.*, **45**, 117.
4 Wintterlin, J., Völkening, S., Janssens, T.V.W., Zambelli, T., and Ertl, G. (1997) *Science*, **278**, 1931.
5 Eigler, D.M. and Schweizer, E.K. (1990) *Nature*, **344**, 524.
6 Pust, S.E., Maier, W., and Wittstock, G. (2008) *Z. Phys. Chem.*, **222**, 1463.
7 Bonnell, D.A. (1993) *Scanning Tunneling Microscopy and Spectroscopy*, VCH, Weinheim.
8 Wiesendanger, R. (1994) *Scanning Probe Microscopy and Spectroscopy*, Cambridge University Press, Cambridge.
9 Güntherodt, H-.J. and Wiesendanger, R. (eds) (1994) *Scanning Tunneling Microscopy I–III*, Springer, Berlin.
10 Wintterlin, J., Wiechers, J., Brune, H., Gritsch, T., Höfer, H., and Behm, R.J. (1989) *Phys. Rev. Lett.*, **62**, 59.
11 Simmons, J.G. (1963) *J. Appl. Phys.*, **34**, 1793.
12 Schmid, M., Stadler, H., and Varga, P. (1993) *Phys. Rev. Lett.*, **70**, 1441.
13 Wouda, P.T., Nieuwenhuys, B.E., Schmid, M., and Varga, P. (1996) *Surf. Sci.*, **359**, 17.
14 Ruff, M., Takehiro, N., Liu, P., Nørskov, J.K., and Behm, R.J. (2007) *ChemPhysChem.*, **8**, 2068.
15 Engelmann, G.E., Ziegler, J.C., and Kolb, D.M. (1998) *Surf. Sci.*, **401**, L420.
16 Kuk, Y. and Silverman, P.J. (1990) *J. Vac. Sci. Technol.*, **A8**, 289.
17 (a) Hugelmann, M. and Schindler, W. (2003) *Surf. Sci.*, **541**, L643; (b) (2004) *J. Electrochem. Soc.*, **151**, E97.
18 Simeone, F.C., Kolb, D.M., Venkatachalam, S., and Jacob, T. (2007) *Angew. Chem. Int. Ed.*, **46**, 8903.
19 Simeone, F.C., Kolb, D.M., Venkatachalam, S., and Jacob, T. (2008) *Surf. Sci.*, **602**, 1401.
20 Kolb, D.M., Nichols, R.J., and Behm, R.J. (1992) *Electrified Interfaces in Physics, Chemistry and Biology, NATO ASI*, Vol. C 355 (ed. R. Guidelli), Kluwer, Dordrecht, p. 275.
21 Wintterlin, J. (1988) PhD Thesis, Free University Berlin.

22 Wiechers, J., Twomey, T., Kolb, D.M., and Behm, R.J. (1988) *J. Electroanal. Chem.*, **248**, 451.

23 Nagahara, L.A., Thundat, T., and Lindsay, S.M. (1989) *Rev. Sci. Instrum.*, **60**, 3128.

24 Bach, C.E., Nichols, R.J., Beckmann, W., Meyer, H., Schulte, A., Besenhard, J.O., and Jannakoudakis, P.D. (1993) *J. Electrochem. Soc.*, **140**, 1281.

25 See, for example, Dakkouri, A.S. (1996) PhD Thesis, University Ulm.

26 Kolb, D.M. (2002) *Advances in Electrochemical Science and Engineering.*, Vol. 7 (eds R.C. Alkire and D.M. Kolb), Wiley-VCH Verlag, Weinheim, p. 107.

27 Pohl, D.W. (1986) *IBM J. Res. Dev.*, **30**, 417.

28 Bockris, J.O'M., Devanathan, M.A.V., and Müller, K. (1963) *Proc. Roy. Soc. Lond.*, A274, 55.

29 Gerischer, H. (1997) *The CRC Handbook of Solid State Electrochemistry*, Chapter 2 (eds P.J. Gellings and H.J.M. Bouwmeester), CRC Press, Boca Raton.

30 Xie, Z.-X. and Kolb, D.M. (2000) *J. Electroanal. Chem.*, **481**, 177.

31 Stimming, U., Vogel, R., Kolb, D.M., and Will, T. (1993) *J. Power Sources*, 43/44, 169.

32 Adzic, R.R., Tripkovic, A.V., and O'Grady, W.E. (1982) *Nature*, **296**, 137.

33 Schultze, J.W. and Dickertmann, D. (1976) *Surf. Sci.*, **54**, 489.

34 Jüttner, K. and Lorenz, W.J. (1980) *Z. Phys. Chem. N.F.*, **122**, 163.

35 Hubbard, A.T. (1973) *Crit. Rev. Anal. Chem.*, **3**, 201.

36 O'Grady, W.E., Woo, M.Y.C., Hagans, P.L., and Yeager, E. (1977) *J. Vac. Sci. Technol.*, **14**, 365.

37 Kolb, D.M. (1987) *Z. Phys. Chem. N.F.*, **154**, 179.

38 Clavilier, J., Faure, R., Guinet, G., and Durand, R. (1980) *J. Electroanal. Chem.*, **107**, 205, 211.

39 Hamelin, A., Doubova, L., Wagner, D., and Schirmer, H. (1987) *J. Electroanal. Chem.*, **220**, 155.

40 Wasberg, M., Palaikis, L., Wallen, S., Kamrath, M., and Wieckowski, A. (1988) *J. Electroanal. Chem.*, **256**, 51.

41 Kibler, L.A., Cuesta, A., Kleinert, M., and Kolb, D.M. (2000) *J. Electroanal. Chem.*, **484**, 73.

42 Kibler, L.A. Preparation and Characterization of Noble Metal Single-Crystal Electrodes, http://www.uni-ulm.de/echem/index.html?id=1023001.

43 Hoyer, R. (2004) PhD Thesis, University Ulm.

44 Magnussen, O.M. (2002) *Chem. Rev.*, **102**, 679.

45 Kibler, L.A., Kleinert, M., and Kolb, D.M. (2000) *Surf. Sci.*, **461**, 155.

46 Waibel, H.-F., Kleinert, M., Kibler, L.A., and Kolb, D.M. (2002) *Electrochim. Acta*, **47**, 1461.

47 Cuesta, A., Kleinert, M., and Kolb, D.M. (2000) *Phys. Chem. Chem. Phys.*, **2**, 5684.

48 Schweizer, M. and Kolb, D.M. (2003) *Surf. Sci.*, **544**, 93.

49 Kibler, L.A., Kleinert, M., Randler, R., and Kolb, D.M. (1999) *Surf. Sci.*, **443**, 19.

50 Maroun, F., Ozanam, F., Magnussen, O., and Behm, R.J. (2001) *Science*, **293**, 1811.

51 Varga, P., Schmid, M., and Redinger, J. (2000) *Physik in Unserer Zeit*, **31**, 215.

52 Diemant, T., Hager, T., Hoster, H.E., Rauscher, H., and Behm, R.J. (2003) *Surf. Sci.*, **541**, 137.

53 Kibler, L.A. and Kolb, D.M. (2003) *Z. Phys. Chem.*, **217**, 1265.

54 El-Aziz, A.M. and Kibler, L.A., in preparation.

55 Nichols, R.J., Bunge, E., Meyer, H., and Baumgärtel, H. (1995) *Surf. Sci.*, **335**, 110.

56 Hoyer, R., Kibler, L.A., and Kolb, D.M. (2003) *Electrochim. Acta*, **49**, 63.

57 Somorjai, G.A. (1977) *Adv. Catal.*, **26**, 1.

58 Lehmpfuhl, G., Uchida, Y., Zei, M.S., and Kolb, D.M. (1999) *Imaging of Surfaces and Interfaces* (eds J. Lipkowski and P.N. Ross), Wiley-VCH Verlag, Weinheim.

59 Cerviño, A.M., Triaca, W.A., and Arvia, A.J. (1985) *J. Electrochem. Soc.*, **132**, 266.

60 Canullo, J.C., Triaca, W.E., and Arvia, A.J. (1984) *J. Electroanal. Chem.*, **175**, 337.

61 Canullo, J., Uchida, Y., Lehmpfuhl, G., Twomey, T., and Kolb, D.M. (1987) *Surf. Sci.*, **188**, 350.

62 Twomey, T.A. (1989) *J. Electroanal. Chem.*, **270**, 465.

63 Schneeweiss, M.A. and Kolb, D.M. (1997) *Solid State Ionics*, **94**, 171.

64 Stickney, J.L., Villegas, I., and Ehlers, C.B. (1989) *J. Am. Chem. Soc.*, **111**, 6473.

65 Will, T., Dietterle, M., and Kolb, D.M. (1995) *Nanoscale Probes of the Solid/Liquid Interface, NATO ASI*, Vol. E288 (eds A.A. Gewirth and H. Siegenthaler), Kluwer, Dordrecht, p. 137.

66 Crommie, M.F., Lutz, C.P., and Eigler, D.M. (1992) *Science*, **262**, 218.

67 Meyer, G., Bartels, L., Zöphel, S., and Rieder, K.H. (1999) *Appl. Phys. A*, **68**, 125.

68 Cuberes, M.T., Schlitter, R.R., and Gimzewski, J.K. (1997) *Surf. Sci.*, **371**, L231.

69 Li, W., Virtanen, J.A., and Penner, R.M. (1992) *Appl. Phys. Lett.*, **60**, 1181.

70 Nyffenegger, R.M. and Penner, R.M. (1997) *Chem. Rev.*, **97**, 1195.

71 Homma, T., Kubo, N., and Osaka, T. (2003) *Electrochim. Acta*, **48**, 3115.

72 Kubo, N., Homma, T., Hondo, Y., and Osaka, T. (2005) *Electrochim. Acta*, **51**, 834.

73 LaGraff, J.R. and Gewirth, A.A. (1994) *J. Phys. Chem.*, **98**, 11246.

74 Petri, M. and Kolb, D.M. (2002) *Phys. Chem. Chem. Phys.*, **4**, 1211.

75 Schindler, W., Hofmann, D., and Kirschner, J. (2001) *J. Electrochem. Soc.*, **148**, C124.

76 Schindler, W., Hofmann, D., and Kirschner, J. (2000) *J. Appl. Phys.*, **87**, 7007.

77 Schindler, W., Hugelmann, P., Hugelmann, M., and Kärtner, F.X. (2002) *J. Electroanal. Chem.*, **522**, 49.

78 Garcia, S.G., Salinas, D.R., Mayer, C.E., Lorenz, W.J., and Staikov, G. (2003) *Electrochim. Acta*, **48**, 1279.

79 Lang, G., Bakos, I., and Horanyi, G. (2000) *J. Electroanal. Chem.*, **493**, 141.

80 Kirchner, V., Cagnon, L., Schuster, R., and Ertl, G. (2001) *Appl. Phys. Lett.*, **79**, 1721.

81 Kirchner, V., Xia, X.H., and Schuster, R. (2001) *Acc. Chem. Res.*, **34**, 371.

82 Schuster, R. and Ertl, G. (2003) *Catalysis and Electrocatalysis at Nanoparticle Surfaces* (eds E. Savinova C. and Vayenas), Marcel Dekker, New York.

83 Avouris, P., Hertel, T., and Martel, R. (1997) *Appl. Phys. Lett.*, **71**, 285.

84 Meier, J., Friedrich, K.A., and Stimming, U. (2002) *Faraday Discuss.*, **121**, 365.

85 Bard, A.J. and Mirkin, M.V. (eds) (2001) *Scanning Electrochemical Microscopy*, Marcel Dekker, New York.

86 Zhou, J., Zu, Y., and Bard, A.J. (2000) *J. Electroanal. Chem.*, **491**, 22.

87 Baltes, N., Thouin, L., Amatore, C., and Heinze, J. (2004) *Angew. Chem. Int. Ed.*, **43**, 1431.

88 Ufheil, J., Hess, C., Borgwarth, K., and Heinze, J. (2005) *Phys. Chem. Chem. Phys.*, **7**, 3185.

89 Landman, U., Luedtke, W.D., Burnham, N.A., and Colton, R.J. (1990) *Science*, **248**, 454.

90 Kolb, D.M., Ullmann, R., and Will, T. (1997) *Science*, **275**, 1097.

91 Kolb, D.M. (2001) *Angew. Chem. Int. Ed.*, **40**, 1162.

92 Kolb, D.M. and Simeone, F.C. (2005) *Electrochim. Acta*, **50**, 2989.

93 Kolb, D.M., Engelmann, G.E., and Ziegler, J.C. (2000) *Solid State Ionics*, **131**, 69.

94 Wang, J.G., Tang, J., Fu, Y.C., Wei, Y.M., Chen, Z.B., and Mao, B.W. (2007) *Electrochem. Commun.*, **9**, 633.

95 Wei, Y.M., Zhou, X.S., Wang, J.G., Tang, J., Mao, B.W., and Kolb, D.M. (2008) *Small*, **4**, 1355.

96 Kolb, D.M., Engelmann, G.E., and Ziegler, J.C. (2000) *Angew. Chem. Int. Ed.*, **39**, 1123.

97 Engelmann, G.E. (1997) PhD Thesis, University Ulm.

98 Endres, F., Abbott, A.P., and MacFarlane, D.R. (eds) (2008) *Electrodeposition from Ionic Liquids*, Wiley-VCH Verlag, Weinheim.

99 Endres, F. (2004) *Z. Phys. Chem.*, **218**, 255.